ACS Sustainable Chemistry & Engineering

pubs.acs.org/journal/ascecg

Research Article

Evaluation of a V_8C_7 Anode for Oxygen Evolution in Alkaline Media: Unusual Morphological Behavior

Kenta Kawashima, Chi L. Cao, Hao Li, Raúl A. Márquez-Montes, Bryan R. Wygant, Yoon Jun Son, Joseph V. Guerrera, Graeme Henkelman, and C. Buddie Mullins*

Cite This: *ACS Sustainable Chem. Eng.* 2020, 8, 14101−14108

Read Online

ACCESS | Metrics & More | Article Recommendations | Supporting Information

ABSTRACT: Metallic vanadium carbide (V_8C_7) with cubic symmetry is examined as an oxygen evolution reaction (OER) precatalyst in alkaline media. Herein, we used quasi in situ scanning electron microscopy and energy-dispersive X-ray spectrometry to investigate the structural transformation of the precatalyst V_8C_7 microparticles during extended cyclic voltammetric (CV) OER testing. Interestingly, an anisotropic morphological transformation (from a distorted sphere to a cuboid) of V_8C_7 was observed. Our theoretical and experimental results strongly suggest that this morphological change happens due to the selective self-oxidation and dissolution of the V_8C_7(110) and (111) surfaces and the subsequent exposure of the relatively stable (100), (010), and (001) surfaces. These results also suggest that these stable facets are preferable for the OER, and a current density of 10 mA·cm^{-2} was delivered at an overpotential of 503 mV after the extended CV OER testing.

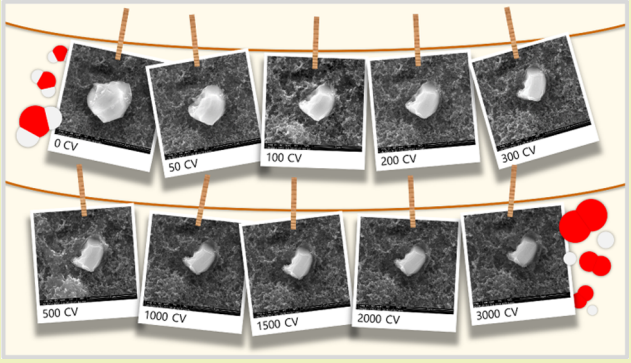

KEYWORDS: *precatalyst, electrocatalyst, oxygen evolution reaction (OER), vanadium carbide, water splitting*

INTRODUCTION

Electrocatalytic water splitting to convert electrical energy into chemical energy is a promising strategy for future energy storage. Overall, water splitting is mainly limited by the sluggish kinetics of the oxygen evolution reaction (OER) rather than by the hydrogen evolution reaction (HER). This is because the four-electron OER involves many intermediates [i.e., HO*, O*, and HOO* (where * denotes a site on the surface)] and is more kinetically challenging than the two-electron HER.[1] To carry out the kinetically difficult OER at a large scale, an earth-abundant electrocatalytic material with high activity and robust stability is essential. Transition metal carbides, borides, pnictides, and chalcogenides (here we refer to these collectively as "TM X-ides") are an interesting class of oxygen evolution electrocatalysts that have been extensively studied over the past several years.[2−9] With the exception of some special cases,[10,11] most TM X-ides undergo partial and/or full oxidation and typically form their TM oxide/(oxy)hydroxide counterparts under OER conditions.[12−18] These TM X-ides are sometimes referred to as "precatalysts," since the newly-formed TM oxide/(oxy)hydroxide acts as the OER active sites rather than the initial TM X-ide. More interestingly, the as-oxidized TM X-ides tend to achieve higher oxygen evolution activity than the corresponding directly synthesized TM oxides/(oxy)hydroxides.[16,17,19] Hence, to understand the OER mechanism on the TM X-ide, pre- and post-OER material characterizations are essential.

Among the above-mentioned TM X-ides, the transformation of TM carbides to the corresponding TM oxides/(oxy)-hydroxides has not been examined thoroughly. So far, several studies providing sufficient pre- and post-OER analyses to identify the final catalyst have reported that, as expected, TM carbide precatalysts undergo partial or full oxidation under OER operations.[13,20−24] However, TM carbide transformation during the OER testing is not always caused by simple self-oxidation but in some cases through a very complicated process. According to a recent report by Yang et al.,[25] the cubic Mo_6Ni_6C precatalyst was transformed into $MoNi_3$, $MoNi_4$, and amorphous carbon under OER conditions. Spontaneously, these MoNi alloys were then partially oxidized into amorphous MoO_x and NiOOH, and the as-formed Mo^{6+}-activated oxide/oxyhydroxide on the surface of MoNi alloys could promote the OER. Accordingly, when a new TM carbide is studied as an OER electrocatalyst, particularly close attention should be paid

Received: June 28, 2020
Revised: July 28, 2020
Published: August 21, 2020

to analyzing any in situ transformations under OER operation in case of unexpected behavior.

In this work, we evaluate cubic vanadium carbide (V_8C_7) microparticles as an OER electrocatalyst in alkaline media. Specifically, the transformation of V_8C_7 under OER operation is monitored using voltammetric analysis, pre- and post-OER X-ray diffraction analysis, and quasi in situ scanning electron microscopy-energy-dispersive X-ray spectrometry analysis. Furthermore, density functional theory (DFT) analysis for the surfaces of the V_8C_7 system is performed to explain the morphological transformation of V_8C_7 during OER testing. Our theoretical and experimental findings suggest that the V_8C_7(100), (010), and (001) surfaces are stable and preferable for the OER, whereas the (110) and (111) surfaces undergo self-oxidation and dissolution under OER conditions. This crystal-face-dependent stability difference induced an anisotropic shape transformation (from a distorted sphere to a cuboid) of the V_8C_7 particle. This work uncovers a new strategy for better understanding X-ide OER precatalysts to enhance their OER activities and stabilities via the control of their crystal growth orientation.

EXPERIMENTAL SECTION

Materials. Vanadium carbide (99% metal basis, Alfa Aesar), potassium hydroxide (86.4%, Fisher Scientific), potassium chloride (99.5%, Fisher Scientific), isopropyl alcohol (isopropanol, 99.9%, Fisher Scientific), Nafion perfluorinated ion-exchange resin solution (5 wt % solution in lower aliphatic alcohols/water mixture, Sigma Aldrich), and carbon black (CB, Hanwha Chemical) were used as received for electrochemical experiments. Ultrapure water (18 MΩ) was used for all aqueous solutions.

Characterization. X-ray diffraction (XRD) patterns of the samples were collected using a Rigaku Miniflex 600 X-ray diffractometer (Rigaku) with Cu Kα radiation (λ = 1.5406 Å). The sample morphologies and sizes were examined by a Quanta 650 environmental scanning electron microscope (ESEM, FEI) with an energy-dispersive X-ray spectrometer (EDX). The Brunauer–Emmett–Teller (BET) specific surface area (S_{BET}) was calculated from N_2-sorption isotherms at 77 K on the powder sample vacuum-degassed at 100 °C for 16 h with a Nova 2200e surface analyzer (Quantachrome).

Electrode Preparation. The CB-supported vanadium carbide thin film (V_8C_7-CB) was fabricated on a glassy carbon (GC) electrode (0.19625 cm^2) via a drop-casting method. First, an ink of vanadium carbide/CB in a 4:1 weight ratio was prepared by ultrasonically dispersing 4 mg of vanadium carbide powder and 1 mg of CB in a 1.0 mL solution (0.98 mL of isopropanol and 0.02 mL of 5 wt % Nafion solution). Subsequently, 24 μL (3 μL × 8) of the as-prepared ink was cast on the GC electrode and dried under an ambient environment. Here, the resultant catalyst (V_8C_7) loading was about 0.49 mg·cm^{-2}. To check the CB contributions on the OER performance and surface area changes during the long-term OER test, the CB thin film was also prepared on a GC electrode by following the above-described procedure without adding the V_8C_7 powder.

Electrochemical Measurements. To evaluate OER performance, the electrochemical measurements of the as-prepared electrodes were conducted in 150 mL of 1 M KOH aqueous solution (pH ~ 14) using a CHI660D electrochemical workstation (CH Instrument) with a standard three-electrode system consisting of the as-prepared V_8C_7-CB/GC or CB/GC working electrode, a platinum coil counter electrode, and a Ag/AgCl (saturated KCl) reference electrode at room temperature. Linear sweep voltammetry (LSV) and cyclic voltammetry (CV) were performed using a rotating disk electrode technique (1600 rpm). All the measurements were compensated by 80% iR-drop.

To investigate the electrode surface area change during the OER test, electrochemically active surface areas (ECSAs) were estimated from the electrochemical double-layer capacitances (C_{dl}s). Cyclic voltammograms (CVs) with different scan rates were obtained in the non-faradic potential window (−0.05 to 0.05 $V_{Ag/AgCl}$) to calculate C_{dl} from the scan-rate dependence of double-layer charging [$\Delta j/2 = (j_a - j_c)/2$].[26] The potentials applied relative to Ag/AgCl were converted into the reversible hydrogen electrode (RHE) scale via the Nernst equation [$E_{RHE} = E_{Ag/AgCl} + 0.0591 \times pH + E_{Ag/AgCl}^0$: $E_{Ag/AgCl}^0$ (saturated KCl) = 0.1976 V at 25 °C].

Computational Methodology. Spin-polarized DFT calculations were performed with the Vienna ab initio simulation package (VASP) code.[27,28] The core electrons were described by the projector augmented-wave method.[29] The valence electrons were described by the Kohn–Sham wave functions expanded in a plane wave basis, with an energy cutoff of 400 eV.[30] The electronic exchange and correlation were described by a generalized gradient approximation with the functional developed by Perdew, Burke, and Ernzerhof.[31] The Brillouin zone was sampled using the Monkhorst–Pack method by a (3 × 3 × 1) k-point mesh.[32] Structures were considered as converged when the forces fell below 0.05 eV·$Å^{-1}$. Stricter criteria were tested in our calculations (e.g., with higher kinetic cutoff and stricter force criteria); no significant change was found in the free energy and adsorption configuration. The V_8C_7 surface was modeled as a V-terminated (100) slab (with a vacuum layer of 12 Å), based upon the fact that the C-terminated surface is relatively inert due to abundant inert C sites. Other possible adsorption sites or surfaces [e.g., the V-terminated (111)] were also tested; none of those surface sites show stable HOO* adsorption. Therefore, only our results on the V_8C_7(100) are present in this study.

RESULTS AND DISCUSSION

Characterization of Microscale V_8C_7. The XRD pattern of the vanadium carbide powder is shown in Figure 1a. The

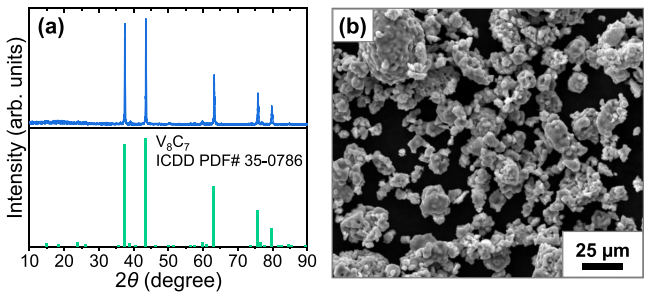

Figure 1. (a) XRD pattern and (b) SEM image of the V_8C_7 powder sample.

diffraction peaks can be indexed as a cubic V_8C_7 phase (ICDD PDF #35-0786) without any diffraction peaks corresponding to impurity phases. The crystal structure of cubic V_8C_7 is available in Figure S1. Figure 1b shows the SEM image of the V_8C_7 powder. As shown, the microscale V_8C_7 particles possessed nonuniform quasi-spherical (less-faceted) shapes with smooth surfaces. Moreover, these V_8C_7 microparticles mostly formed relatively large agglomerates.

In general, metal carbides are thermodynamically less stable than their oxide counterparts in the presence of oxidants (O_2, H_2O, etc.).[2,33,34] According to previous reports,[35−39] TM carbides tend to undergo the unavoidable oxidation at their surfaces before OER testing. To check the oxidation degree and rough chemical composition of the initial vanadium carbide microparticle, EDX point analysis was carried out (see Figure S2). For this analysis, the maximum electron acceleration voltage of 30 kV was used to gain information from inside the particle. There was a small amount of O, possibly indicating that only the V_8C_7 microparticle surface

https://dx.doi.org/10.1021/acssuschemeng.0c04759
ACS Sustainable Chem. Eng. 2020, 8, 14101−14108

was partially oxidized by exposure to ambient air. The as-obtained C/V atomic ratio (~1.13) was slightly higher than the theoretical value (0.875) in V_8C_7. As shown in Figure S3, some of the V_8C_7 microparticles showed exfoliated thin layers on their surfaces. Generally, regardless of synthesis methods, thin carbon layers tend to form on the resultant TM carbides.[26,40−42] Accordingly, the as-observed thin layers on the V_8C_7 sample may correspond to carbon, which might be the reason for the unexpected high C/V atomic ratio. Regardless, the relatively low (<3 atom %) oxygen content indicates the particle is largely unoxidized from their mild exposure to air. The S_{BET} of V_8C_7 microparticles was also obtained via the multipoint BET analysis from the N_2-adsorption isotherm (Figure S4). The resultant S_{BET} value was 0.389 $m^2 \cdot g^{-1}$, showing good agreement with the SEM result. Notably, it was confirmed that the V_8C_7 sample is in good condition for further electrochemical measurements.

Electrochemistry and Catalysis in the V_8C_7 Anode. The OER performance of the V_8C_7-CB/GC electrode was investigated by voltammetric measurements using a three-electrode system. To evaluate the effects of the support and substrate materials on the electrochemical results, a CB/GC electrode without the carbide electrocatalyst was tested as well. First, the ECSAs of V_8C_7-CB/GC and CB/GC were estimated from their CV-derived C_{dl} values. As shown in Figure S5, the C_{dl} value of V_8C_7-CB/GC (0.299 $mF \cdot cm^{-2}$) is slightly higher than that of CB/GC (0.262 $mF \cdot cm^{-2}$); this C_{dl} difference seemingly corresponds to the C_{dl} value of the loaded V_8C_7 microparticles ($C_{dl,VC}$). Prior to the measurements of the linear polarization curves to check the OER overpotentials (η) at a current density of 10 $mA \cdot cm^{-2}$, the electrodes were activated by performing LSV until minimal changes were observed between consecutive sweeps (Figure S6). Previous studies regarding nonoxide TM-based precatalysts have shown that irreversible oxidation peaks, in which the precatalysts themselves were electrooxidized, were observed in an initial voltammetric activation sweep/cycle.[13,17,43] However, in the first sweep of the linear polarization curve for V_8C_7-CB/GC, there seems to be no distinct oxidation peak. This can be interpreted via three possible reasons: (i) no surface change of the V_8C_7, (ii) a small degree of V_8C_7 oxidation, or (iii) another side reaction, which removes the oxidized vanadium species away from the V_8C_7 surface (i.e., V_8C_7 dissolution). This latter point will be discussed in greater detail later in the paper. After the LSV activation, the overpotential of V_8C_7-CB/GC was 458 mV at 10 $mA \cdot cm^{-2}$, whereas CB/GC could not reach the current density of 10 $mA \cdot cm^{-2}$ within the recorded potential window (see Figure S7). As seen in Figures S5, S8, and S9, there were no significant changes in the ECSAs of both electrodes before and after the LSV activation, implying that there are very few changes in the surface morphologies of both electrodes during the LSV activation.

To elucidate the transformation behavior of the V_8C_7 under oxidative conditions, we conducted continuous OER CV scans between 1.10 and 1.65 V_{RHE} at 50 $mV \cdot s^{-1}$ on the V_8C_7-CB/GC and CB/GC electrodes. Here, changes in the OER overpotential and CV-derived C_{dl} were monitored as a function of the CV cycle number (Figures 2 and S7−9). In Figures 2 and S7a, we observe a decline in the OER activity of V_8C_7-CB/GC, with a gradual overpotential increase of ~0.078 $mV \cdot cycle^{-1}$ during the first 500 cycles. After that, the overpotential of the V_8C_7-CB/GC remained almost unchanged (~500 mV) until the completion of 3000 cycles. On the other hand, the LSV

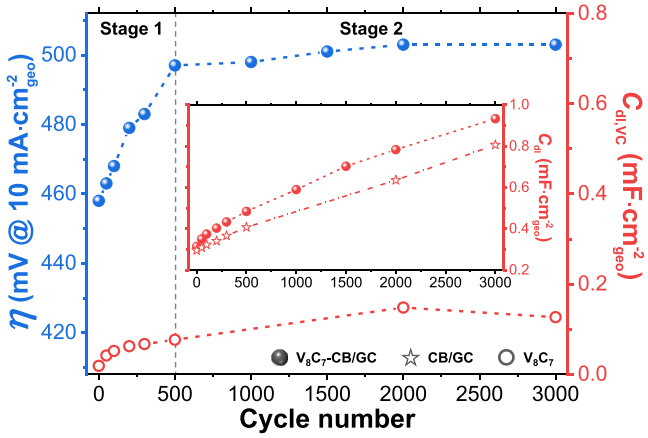

Figure 2. Trend of OER overpotential (blue) and double-layer capacitance (red) versus the cycle number of CV for the V_8C_7-CB/GC and CB/GC electrodes. Multi-CV was performed in the potential range of 1.10 to 1.65 V_{RHE} with a scan rate of 50 $mV \cdot s^{-1}$ for 3000 cycles in 1 M KOH aqueous solution.

curve of CB/GC displayed no significant change after 500 cycles (see Figure S7b). However, after 2000 and 3000 cycles, current densities at greater than ~1.6 V_{RHE} increased. Recently, studies by Wang et al. and Suryanto et al. reported that the OER performance of CB can be enhanced by its electro-oxidation.[44,45] Therefore, the same effect could have happened in our CB/GC case. In addition, this improvement of the CB activity for the OER contributed to some extent in the maintenance of the OER activity of V_8C_7-CB/GC at high cycle numbers. As depicted in the inset of Figure 2, for V_8C_7-CB/GC, the C_{dl} value continuously increased throughout the entire CV test. A similar phenomenon observed for CB/GC can be assigned to the interlayer space expansion of graphitic CB due to its electrochemically induced intercalation and exfoliation.[44] Hence, the C_{dl} increase in V_8C_7-CB/GC is mainly assignable to this CB interlayer expansion. As mentioned above, the relatively small difference in C_{dl} between V_8C_7-CB/GC and CB/GC is primarily attributed to the $C_{dl,VC}$. At 0−500 cycles, the highest rate of $C_{dl,VC}$ increase was recorded; the $C_{dl,VC}$ at 500 cycles (76.6 $\mu F \cdot cm^{-2}$) is roughly four times larger than at 0 cycles (18.7 $\mu F \cdot cm^{-2}$). Afterward, $C_{dl,VC}$ increased about twofold from 500 to 2000 cycles. Finally, the $C_{dl,VC}$ peaked at 2000 cycles, showing no significant changes from 2000 to 3000 cycles. Taken together, these electrochemical results suggest that the V_8C_7 undergoes a morphological transformation of some sort during the continuous OER CV scans.

To acquire a better interpretation of the above electrochemical data, we performed a quasi in situ SEM-EDX analysis of the morphological and compositional changes in the V_8C_7 microparticles during continuous OER CV scans. Specifically, the SEM and EDX mapping images of V_8C_7 microparticles [on the V_8C_7-CB/Ti foil electrode (see Figure S10); preparation details in the Supporting Information (SI)] were collected at various intervals over 3000 cycles. As displayed in Figure 3, a gradual reduction in the size of the V_8C_7 microparticle was clearly confirmed over the cycle range of 0 to 500. This gradual size reduction was likely caused by the partial dissolution of V_8C_7 that likely resulted from the oxidation of V_8C_7 into vanadium oxide (as typified by V_2O_5).[46,47] The as-formed V_2O_5 can then readily dissolve in the electrolyte as VO_4^{3-}.[48] Interestingly, during the course of this process, the initial particle seemed to anisotropically transform from a rounded

https://dx.doi.org/10.1021/acssuschemeng.0c04759
ACS Sustainable Chem. Eng. 2020, 8, 14101−14108

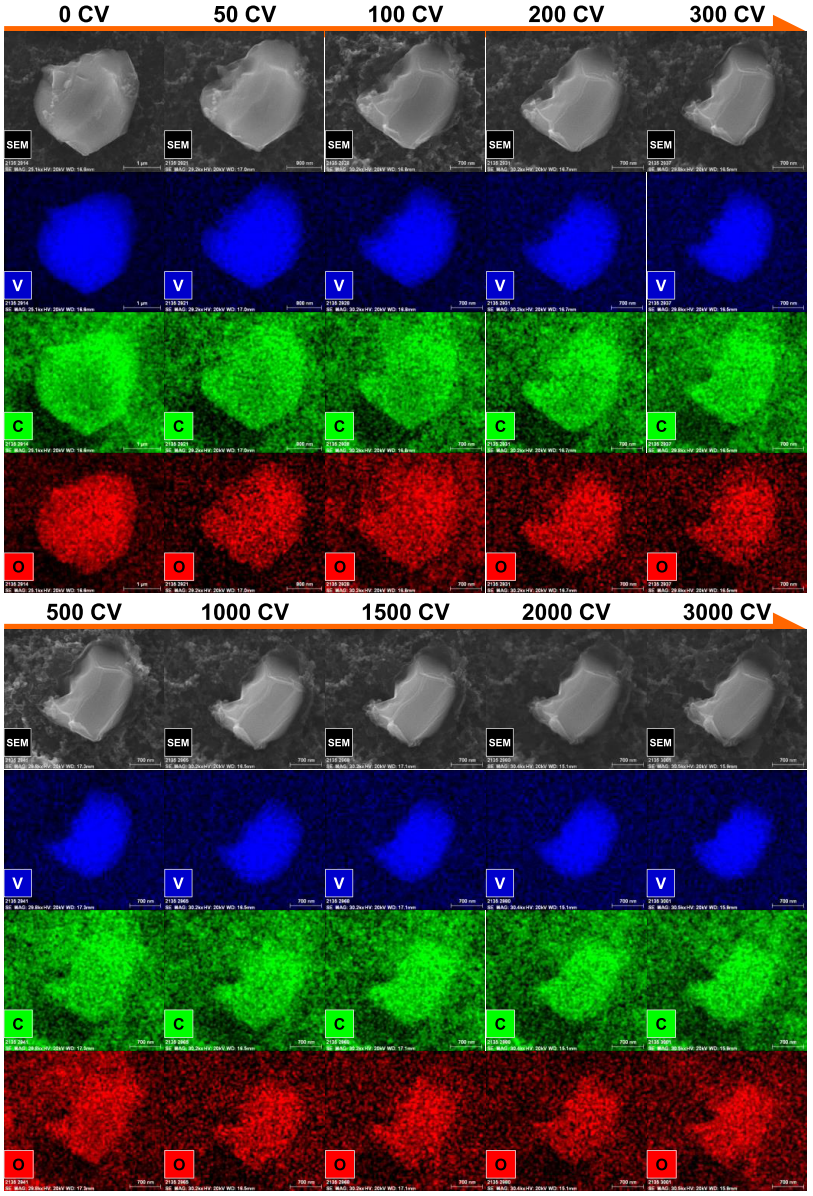

Figure 3. Quasi in situ SEM and EDX elemental mapping images (accelerating voltage: 20 kV) of the V_8C_7 particle (in the V_8C_7-CB/Ti electrode) before and after the various cycle numbers of the OER CV (1.10 to 1.65 V_{RHE}) at the scan rate of 50 $mV \cdot s^{-1}$.

particle into a well-faceted particle with a cuboid-like shape, as seen in Figure 3. After 500 cycles, the particle size and morphology underwent little change with further CV cycling (500 to 3000 cycles). Importantly, this dissolution suppression is not caused by the saturation of vanadium in the electrolyte (details in the SI). Based on these observations, it is presumed that the oxidation resistivity of V_8C_7 differs depending on the crystal facet. Figure 3 shows the quasi in situ EDX elemental maps of the V_8C_7 microparticle (the corresponding pre- and post-OER EDX spectra is also available in Figure S11). In all of the maps, the strong V (blue) and C (green) signals were evenly distributed throughout the V_8C_7 microparticle, indicating that the V_8C_7 composition might be mainly kept throughout the particle, during the OER cycling. The oxygen (red), with roughly visually constant signal strength, was also confirmed over 3000 cycles, which may correspond to the surface oxidation of the V_8C_7 microparticle. Furthermore, to confirm the above results, we performed the same CV test (3000 cycles) and the pre- and post-OER analysis on a relatively large V_8C_7 microparticle. As seen in Figure S12, the development of crystal facets and edges was again observed after 3000 cycles. The corresponding EDX elemental mapping analysis also showed similar results to those shown in Figure 3 (see Figure S12). To reveal the degree of its surface oxidation, the EDX point analysis of the V_8C_7 microparticle before and after 3000 cycles was conducted (Figure S13). The resultant O/V atomic ratios were 0.27 and 0.22 for the pre- and post-OER samples, respectively. Hence, only the outermost surface of the post-OER V_8C_7 microparticle was oxidized, even after long OER CV scans.

To further examine the crystallographic change, XRD measurements were used to analyze the pre- and post-OER V_8C_7-CB/Ti electrodes. As shown in Figure 4a, the diffraction peaks of both the pre- and post-OER electrodes can be assigned to cubic V_8C_7 and hexagonal Ti (ICDD PDF #44-1294). There are no diffraction peaks corresponding to oxidized V_8C_7 phases, suggesting that the partial oxidation indeed happens on the outermost surface of the post-OER

https://dx.doi.org/10.1021/acssuschemeng.0c04759
ACS Sustainable Chem. Eng. 2020, 8, 14101−14108

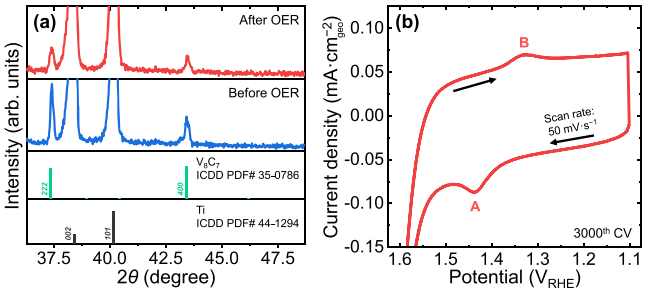

Figure 4. (a) XRD patterns of the V_8C_7-CB/Ti electrode before and after the 3000 cycles of the OER CV (1.10 to 1.65 V_{RHE}). (b) 3000th cyclic voltammogram of the V_8C_7-CB/GC electrode.

V_8C_7, and the as-generated oxidized vanadium species exist in poorly crystalline and amorphous forms. This agrees with the results from the EDX point analysis (Figure S13). Additionally, all of the diffraction peak intensities [relative to the Ti (101) peak intensity] assignable to V_8C_7 slightly decreased after 3000 cycles, which is because of the partial dissolution of V_8C_7 (see Figure 3). More importantly, the decreasing degree of the diffraction peak intensity differs from one crystal facet to another; the peak intensity of (222) seemingly decreased more compared to that of (400). In particular, the intensity ratio of the (222) peak to the (400) peak decreased from 1.25 to 0.89 after 3000 cycles. Based on these XRD results, {111} facets might be selectively dissolved during the OER process, which supports our hypothesis about the anisotropic transformation of the V_8C_7 microparticle shape.

To identify the oxidized vanadium species generated on the V_8C_7 outermost surface, we inspected the magnified 3000th OER CV curve for the V_8C_7-CB/GC electrode. As indicated in Figure 4b, both anodic and cathodic peaks (A and B) were confirmed in the magnified CV curve. According to the report by Shi et al.,[49] the lepidocrocite-type layered vanadium oxyhydroxide (VOOH) electrocatalyst also exhibited a similar anodic peak, which is likely attributed to the V^{3+}-to-V^{5+} oxidation, observed during the OER in alkaline media (1 M KOH). Accordingly, in our case, a similar layered VOOH may form on the outermost surface of V_8C_7 during the OER.

To understand the observed morphological transformation of the V_8C_7 precatalyst, we conducted DFT calculations for cubic V_8C_7. Specifically, a few V-terminated V_8C_7 crystal facets [i.e., (100) and (111)] were simulated. In our calculations, only the V_8C_7(100) surface has a stable HOO* adsorption energy, whereas the V_8C_7(111) facet indicates a difficulty in the formation of stabilized HOO*. Thus, the (100) surface is determined to be more suitable for the OER than the (111) surface. In particular, as shown in Figure 5a, the V_8C_7(100) surface can easily be covered with HO* and O*, since the first step is exothermic. In contrast, the subsequent formation of HOO* is relatively endothermic. Thereby, the partial oxidation of V_8C_7 to V−O−OH may also happen during the OER. In contrast, as none of the stable HOO* configurations were found on the V_8C_7(111) surface, severe self-oxidation of the V_8C_7(111) surface presumably proceeds instead of the OER, consistent with our pre- and post-OER XRD results. Recently, Wan et al. also analyzed the OER activity of V_8C_7 via DFT calculations.[50] According to their results, the (001) surface is predicted to exhibit a higher OER performance than their analyzed higher-index surfaces. Incidentally, the OER activity of their calculated (001) is similar to that of our V-terminated (100); the theoretical onset [(the potential-determining step)/e − 1.23 V] for the (100) surface, which we calculated (~2 V), is close to that for the (001) surface (~1.80 V).[50] Additionally, it is expected that the (010) surface has a similar behavior with (100) and (001) surfaces because the coordination numbers and the appearances of the (001), (010), and (001) surfaces are quite similar in cubic V_8C_7 (see Figure S14). Moreover, since both (110) and (111) have a higher surface index than (100), (110) probably behaves similar to (111). Taken together, the (100), (010), and (001) surfaces are expected to readily carry out the OER, while the (110) and (111) surfaces are not suitable for the OER and may undergo strong self-oxidation instead. We note that to quantify the coverage of each adsorbate on each facet, surface Pourbaix diagram analysis is a more quantified method.[51] However, due to the tremendous computational cost in these calculations, we did not further perform these analyses in our current study.

Finally, on the basis of our findings as well as previous studies, we propose a possible mechanism for the OER precatalytic behavior of V_8C_7 (Figure 5b) in connection with the trends of OER overpotentials and CV-derived $C_{dl,VC}$s versus cycle number (Figure 2) and the quasi in situ SEM-EDX results (Figure 3). During the OER process for V_8C_7, there are two competitive events: (i) the OER and (ii) the severe self-oxidation of V_8C_7. At the V_8C_7(110) and (111) surfaces, the dominant event is the severe self-oxidation of V_8C_7 inducing the dissolution of oxidized vanadium species into the electrolyte as VO_4^{3-} ions.[48] At the V_8C_7(100), (010),

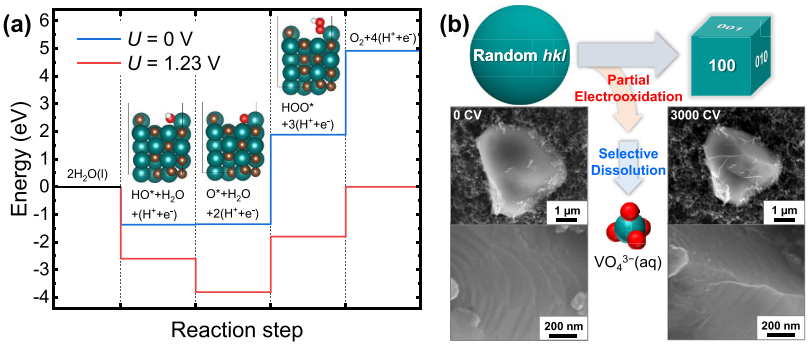

Figure 5. (a) Calculated OER reaction free energy pathway on V_8C_7(100). (b) Schematic illustration of the proposed transformation mechanism of the V_8C_7 particle. SEM images of pre- and post-OER V_8C_7 particles on the V_8C_7-CB/Ti electrode. Note that a roundish shape bounded by random facets is likely transformed into an idiomorphic shape primarily bounded by (100), (010), and (001) facets during the multicyclic voltammetric OER test. Blue, brown, red, and white spheres represent V, C, O, and H atoms, respectively.

https://dx.doi.org/10.1021/acssuschemeng.0c04759
ACS Sustainable Chem. Eng. 2020, 8, 14101−14108

and (001) surfaces, the OER dominantly happens with the partial surface oxidation of V_8C_7 into layered VOOH. In stage 1 (see Figure 2), the OER overpotential gradually increases as the total loading of electrocatalyst decreases, a result of the severe self-oxidation and subsequent dissolution of the V_8C_7(110) and (111) surfaces. The oxidation and subsequent dissolution continue until primarily V_8C_7(100), (010), and (001) surfaces are exposed. Subsequently, layered VOOH active species form on the V_8C_7 (100), (010), and (001) surfaces, resulting in the drastic increase of the $C_{dl,VC}$ value. In stage 2, the self-oxidation and subsequent dissolution of the carbide material are suppressed in accordance with the exposure of the relatively stable (100), (010), and (001) surfaces of V_8C_7. At the same time, the plots of OER overpotentials and $C_{dl,VC}$s gradually level off as the material loss slows. Likewise, the anisotropic transformation of the V_8C_7 microparticle shape (distorted sphere → cuboid) was observed in the quasi in situ SEM analysis (see Figure 3). The facet and edge development on the V_8C_7 microparticle was also confirmed (see Figure 5b). After 3000 cycles, the V_8C_7-CB/GC electrode reached an overpotential of 503 mV at 10 mA·cm^{-2}, relatively high compared to current state-of-the-art electrocatalysts.[52] Moreover, our calculation also suggests that the pristine V_8C_7 surface does not have excellent OER intrinsic activity with a relatively high onset (~2 V). Importantly, however, our findings provide some possible clues to the design of V_8C_7 precatalysts for further improving their geometric OER activity and durability. For example, V_8C_7 nanocubes bounded with (100), (010), and (001) facets may be able to achieve both high geometric OER activity and stability, and the work in this area is currently ongoing.

In this study, we have learned the principles of selective etching in TM X-ide by using V_8C_7 as a model system. Interestingly, a small amount of its oxide counterpart (i.e., VOOH) seemingly formed on the post-OER V_8C_7 surface, which might cause overestimation of the oxidation resistance of V_8C_7 without the quasi in situ SEM-EDX analysis; (quasi) in situ analytical techniques are essential to elucidate the real behavior of a V_8C_7-type OER precatalyst. Furthermore, we hope that this study will provide some clues for opening up novel pathways for understanding the behavior of other possibly interesting TM X-ide systems.

CONCLUSIONS

In summary, microsized vanadium carbide (V_8C_7) was investigated as a potential nonprecious metal precatalyst for the OER in alkaline media. In the quasi in situ SEM-EDX analysis, the trend in the anisotropic shape transition (distorted sphere → cuboid) of the V_8C_7 microparticle was confirmed. Furthermore, according to the pre- and post-OER XRD, DFT calculations, and post-OER CV results, we proposed a possible mechanism for this shape transformation. In the initial stage of OER testing, the V_8C_7(110) and (111) surfaces are strongly oxidized into their oxyanion counterparts under the oxidizing potentials necessary for water oxidation. Subsequently, these oxyanions are continuously dissolved in the electrolyte as VO_4^{3-}. The increased exposure of the V_8C_7(100), (010), and (001) surfaces follows on the heels of this continuous dissolution. Being relatively stable to oxidation, it is at the (100), (010), and (001) surfaces of V_8C_7 that the OER primarily occurs. Simultaneously, a layered VOOH is likely generated on the as-exposed V_8C_7 outermost surfaces, increasing the double-layer capacitance of the V_8C_7 surface. After dissolution ceases and the stable facets predominate, a relatively poor OER activity (η = 503 mV at 10 mA·cm^{-2}) is demonstrated on the post-OER V_8C_7 with well-developed facets and edges. Based on our findings, (100)-, (010)-, and (001)-faceted V_8C_7 nanoparticles would be expected to demonstrate improved catalyst activity and stability, providing an avenue for future research into this understudied class of materials.

ASSOCIATED CONTENT

Supporting Information

The Supporting Information is available free of charge at https://pubs.acs.org/doi/10.1021/acssuschemeng.0c04759.

Experimental details, schematic illustrations, additional SEM-EDX results, SEM images, N_2-sorption isotherm, LSVs, CVs, and digital photographs (PDF)

AUTHOR INFORMATION

Corresponding Author

C. Buddie Mullins − *Department of Chemistry, John J. McKetta Department of Chemical Engineering, and Center for Electrochemistry, The University of Texas at Austin, Austin, Texas 78712, United States;* orcid.org/0000-0003-1030-4801; Email: mullins@che.utexas.edu

Authors

Kenta Kawashima − *Department of Chemistry, The University of Texas at Austin, Austin, Texas 78712, United States;* orcid.org/0000-0001-7318-6115

Chi L. Cao − *John J. McKetta Department of Chemical Engineering, The University of Texas at Austin, Austin, Texas 78712, United States*

Hao Li − *Department of Chemistry and Oden Institute for Computational Engineering and Sciences, The University of Texas at Austin, Austin, Texas 78712, United States*

Raúl A. Márquez-Montes − *Department of Chemistry, The University of Texas at Austin, Austin, Texas 78712, United States;* orcid.org/0000-0003-3885-5007

Bryan R. Wygant − *Department of Chemistry, The University of Texas at Austin, Austin, Texas 78712, United States*

Yoon Jun Son − *John J. McKetta Department of Chemical Engineering, The University of Texas at Austin, Austin, Texas 78712, United States*

Joseph V. Guerrera − *Department of Chemistry, The University of Texas at Austin, Austin, Texas 78712, United States*

Graeme Henkelman − *Department of Chemistry and Oden Institute for Computational Engineering and Sciences, The University of Texas at Austin, Austin, Texas 78712, United States;* orcid.org/0000-0002-0336-7153

Complete contact information is available at: https://pubs.acs.org/10.1021/acssuschemeng.0c04759

Notes

The authors declare no competing financial interest.

ACKNOWLEDGMENTS

The authors gratefully acknowledge the support of the National Science Foundation via grant CHE-1664941 (C.B.M.) for the experimental portion of the paper and the U.S. Department of Energy Basic Energy Sciences Grant DE-SC0010576 (G.H.) for the computational portion of the study. We also acknowledge the Welch Foundation for its generous

support through grants F-1436 (C.B.M.) and F-1841 (G.H.). Computational resources were provided by the Texas Advanced Computing Center and the National Energy Research Scientific Computing Center.

REFERENCES

(1) Koper, M. T. M. Thermodynamic Theory of Multi-Electron Transfer Reactions: Implications for Electrocatalysis. *J. Electroanal. Chem.* **2011**, *660*, 254−260.
(2) Wygant, B. R.; Kawashima, K.; Mullins, C. B. Catalyst or Precatalyst? The Effect of Oxidation on Transition Metal Carbide, Pnictide, and Chalcogenide Oxygen Evolution Catalysts. *ACS Energy Lett.* **2018**, *3*, 2956−2966.
(3) Dinh, K. N.; Liang, Q.; Du, C.-F.; Zhao, J.; Tok, A. I. Y.; Mao, H.; Yan, Q. Nanostructured Metallic Transition Metal Carbides, Nitrides, Phosphides, and Borides for Energy Storage and Conversion. *Nano Today* **2019**, *25*, 99−121.
(4) Joo, J.; Kim, T.; Lee, J.; Choi, S.-I.; Lee, K. Morphology-Controlled Metal Sulfides and Phosphides for Electrochemical Water Splitting. *Adv. Mater.* **2019**, *31*, No. 1806682.
(5) Li, W.; Xiong, D.; Gao, X.; Liu, L. The Oxygen Evolution Reaction Enabled by Transition Metal Phosphide and Chalcogenide Pre-Catalysts with Dynamic Changes. *Chem. Commun.* **2019**, *55*, 8744−8763.
(6) Li, Y.; Du, X.; Huang, J.; Wu, C.; Sun, Y.; Zou, G.; Yang, C.; Xiong, J. Recent Progress on Surface Reconstruction of Earth-Abundant Electrocatalysts for Water Oxidation. *Small* **2019**, *15*, No. 1901980.
(7) Masa, J.; Schuhmann, W. The Role of Non-Metallic and Metalloid Elements on the Electrocatalytic Activity of Cobalt and Nickel Catalysts for the Oxygen Evolution Reaction. *ChemCatChem* **2019**, *11*, 5842−5854.
(8) Sivanantham, A.; Ganesan, P.; Vinu, A.; Shanmugam, S. Surface Activation and Reconstruction of Non-Oxide-Based Catalysts Through in Situ Electrochemical Tuning for Oxygen Evolution Reactions in Alkaline Media. *ACS Catal.* **2020**, *10*, 463−493.
(9) Chen, Z.; Duan, X.; Wei, W.; Wang, S.; Zhang, Z.; Ni, B.-J. Boride-Based Electrocatalysts: Emerging Candidates for Water Splitting. *Nano Res.* **2020**, *13*, 293−314.
(10) Swesi, A. T.; Masud, J.; Nath, M. Nickel Selenide as a High-Efficiency Catalyst for Oxygen Evolution Reaction. *Energy Environ. Sci.* **2016**, *9*, 1771−1782.
(11) De Silva, U..; Masud, J.; Zhang, N.; Hong, Y.; Liyanage, W. P. R.; Zaeem, M. A.; Nath, M. Nickel Telluride as a Bifunctional Electrocatalyst for Efficient Water Splitting in Alkaline Medium. *J. Mater. Chem. A* **2018**, *6*, 7608−7622.
(12) Guo, F.; Wu, Y.; Chen, H.; Liu, Y.; Yang, L.; Ai, X.; Zou, X. High-Performance Oxygen Evolution Electrocatalysis by Boronized Metal Sheets with Self-Functionalized Surfaces. *Energy Environ. Sci.* **2019**, *12*, 684−692.
(13) Kim, J.-H.; Kawashima, K.; Wygant, B. R.; Mabayoje, O.; Liu, Y.; Wang, J. H.; Mullins, C. B. Transformation of a Cobalt Carbide (Co_3C) Oxygen Evolution Precatalyst. *ACS Appl. Energy Mater.* **2018**, *1*, 5145−5150.
(14) Liu, T.; Li, M.; Bo, X.; Zhou, M. Comparison Study toward the Influence of the Second Metals Doping on the Oxygen Evolution Activity of Cobalt Nitrides. *ACS Sustainable Chem. Eng.* **2018**, *6*, 11457−11465.
(15) Xu, X.; Li, C.; Lim, J. G.; Wang, Y.; Ong, A.; Li, X.; Peng, E.; Ding, J. Hierarchical Design of NiOOH@Amorphous Ni−P Bilayer on a 3D Mesh Substrate for High-Efficiency Oxygen Evolution Reaction. *ACS Appl. Mater. Interfaces* **2018**, *10*, 30273−30282.
(16) Mabayoje, O.; Shoola, A.; Wygant, B. R.; Mullins, C. B. The Role of Anions in Metal Chalcogenide Oxygen Evolution Catalysis: Electrodeposited Thin Films of Nickel Sulfide as "Pre-Catalysts.". *ACS Energy Lett.* **2016**, *1*, 195−201.
(17) Chen, W.; Liu, Y.; Li, Y.; Sun, J.; Qiu, Y.; Liu, C.; Zhou, G.; Cui, Y. In Situ Electrochemically Derived Nanoporous Oxides from Transition Metal Dichalcogenides for Active Oxygen Evolution Catalysts. *Nano Lett.* **2016**, *16*, 7588−7596.
(18) Wygant, B. R.; Poterek, A. H.; Burrow, J. N.; Mullins, C. B. Effect of Selenium Content on Nickel Sulfoselenide-Derived Nickel (Oxy)Hydroxide Electrocatalysts for Water Oxidation. *ACS Appl. Mater. Interfaces* **2020**, *12*, 20366−20375.
(19) Xu, X.; Song, F.; Hu, X. A Nickel Iron Diselenide-Derived Efficient Oxygen-Evolution Catalyst. *Nat. Commun.* **2016**, *7*, No. 12324.
(20) Das, D.; Santra, S.; Nanda, K. K. In Situ Fabrication of a Nickel/Molybdenum Carbide-Anchored N-Doped Graphene/CNT Hybrid: An Efficient (Pre)Catalyst for OER and HER. *ACS Appl. Mater. Interfaces* **2018**, *10*, 35025−35038.
(21) He, B.; Kuang, P.; Li, X.; Chen, H.; Yu, J.; Fan, K. In Situ Transformation of Prussian-Blue Analogue-Derived Bimetallic Carbide Nanocubes by Water Oxidation: Applications for Energy Storage and Conversion. *Chem. - Eur. J.* **2019**, *26*, 4052−4062.
(22) Kim, M.; Kim, S.; Song, D.; Oh, S.; Chang, K. J.; Cho, E. Promotion of Electrochemical Oxygen Evolution Reaction by Chemical Coupling of Cobalt to Molybdenum Carbide. *Appl. Catal., B.* **2018**, *227*, 340−348.
(23) Wang, Y.; Wu, W.; Rao, Y.; Li, Z.; Tsubaki, N.; Wu, M. Cation Modulating Electrocatalyst Derived from Bimetallic Metal−Organic Frameworks for Overall Water Splitting. *J. Mater. Chem. A* **2017**, *5*, 6170−6177.
(24) Yang, H.; Luo, S.; Li, X.; Li, S.; Jin, J.; Ma, J. Controllable Orientation-Dependent Crystal Growth of High-Index Faceted Dendritic $NiC_{0.2}$ Nanosheets as High-Performance Bifunctional Electrocatalysts for Overall Water Splitting. *J. Mater. Chem. A* **2016**, *4*, 18499−18508.
(25) Zu, M. Y.; Wang, C.; Zhang, L.; Zheng, L. R.; Yang, H. G. Reconstructing Bimetallic Carbide Mo_6Ni_6C for Carbon Interconnected MoNi Alloys to Boost Oxygen Evolution Electrocatalysis. *Mater. Horiz.* **2019**, *6*, 115−121.
(26) Kawashima, K.; Shin, K.; Wygant, B. R.; Kim, J.-H.; Cao, C. L.; Lin, J.; Son, Y. J.; Liu, Y.; Henkelman, G.; Mullins, C. B. Cobalt Metal−Cobalt Carbide Composite Microspheres for Water Reduction Electrocatalysis. *ACS Appl. Energy Mater.* **2020**, *3*, 3909−3918.
(27) Sun, G.; Kürti, J.; Rajczy, P.; Kertesz, M.; Hafner, J.; Kresse, G. Performance of the Vienna Ab Initio Simulation Package (VASP) in Chemical Applications. *J. Mol. Struct.: THEOCHEM* **2003**, *624*, 37−45.
(28) Hafner, J. Ab-Initio Simulations of Materials Using VASP: Density-Functional Theory and Beyond. *J. Comput. Chem.* **2008**, *29*, 2044−2078.
(29) Blöchl, P. E. Projector Augmented-Wave Method. *Phys. Rev. B* **1994**, *50*, 17953−17979.
(30) Kohn, W.; Sham, L. J. Self-Consistent Equations Including Exchange and Correlation Effects. *Phys. Rev.* **1965**, *140*, A1133.
(31) Perdew, J. P.; Burke, K.; Ernzerhof, M. Generalized Gradient Approximation Made Simple. *Phys. Rev. Lett.* **1996**, *77*, 3865−3868.
(32) Monkhorst, H.; Pack, J. Special Points for Brillouin Zone Integrations. *Phys. Rev. B* **1976**, *13*, 5188−5192.
(33) Niessen, A. K.; De Boer, F. R. The Enthalpy of Formation of Solid Borides, Carbides, Nitrides, Silicides and Phosphides of Transition and Noble Metals. *J. Less-Common Met.* **1981**, *82*, 75−80.
(34) Stevanović, V.; Lany, S.; Zhang, X.; Zunger, A. Correcting Density Functional Theory for Accurate Predictions of Compound Enthalpies of Formation: Fitted Elemental-Phase Reference Energies. *Phys. Rev. B* **2012**, *85*, No. 115104.
(35) Jiang, J.; Liu, Q.; Zeng, C.; Ai, L. Cobalt/Molybdenum Carbide@N-Doped Carbon as a Bifunctional Electrocatalyst for Hydrogen and Oxygen Evolution Reactions. *J. Mater. Chem. A* **2017**, *5*, 16929−16935.
(36) Anjum, M. A. R.; Lee, M. H.; Lee, J. S. Boron- and Nitrogen-Codoped Molybdenum Carbide Nanoparticles Imbedded in a BCN Network as a Bifunctional Electrocatalyst for Hydrogen and Oxygen Evolution Reactions. *ACS Catal.* **2018**, *8*, 8296−8305.

https://dx.doi.org/10.1021/acssuschemeng.0c04759
ACS Sustainable Chem. Eng. 2020, 8, 14101−14108

(37) Ai, L.; Su, J.; Wang, M.; Jiang, J. Bamboo-Structured Nitrogen-Doped Carbon Nanotube Coencapsulating Cobalt and Molybdenum Carbide Nanoparticles: An Efficient Bifunctional Electrocatalyst for Overall Water Splitting. *ACS Sustainable Chem. Eng.* **2018**, *6*, 9912−9920.
(38) Lei, X.; Ye, Z.; Zhao, N.; Lei, F.; Yang, H. Magnetic γ'-Fe_4N/Fe_3C, χ-Fe_5C_2, and θ-Fe_3C by a Simple Route for Application as Electrochemical Catalysts. *Chem. - Eur. J.* **2017**, *23*, 17592−17597.
(39) Jia, X.; Wang, M.; Liu, G.; Wang, Y.; Yang, J.; Li, J. Mixed-Metal MOF-Derived Co-Doped Ni_3C/Ni NPs Embedded in Carbon Matrix as an Efficient Electrocatalyst for Oxygen Evolution Reaction. *Int. J. Hydrogen Energy* **2019**, *44*, 24572−24579.
(40) Fan, X.; Peng, Z.; Ye, R.; Zhou, H.; Guo, X. M_3C (M: Fe, Co, Ni) Nanocrystals Encased in Graphene Nanoribbons: An Active and Stable Bifunctional Electrocatalyst for Oxygen Reduction and Hydrogen Evolution Reactions. *ACS Nano* **2015**, *9*, 7407−7418.
(41) Kang, J. S.; Kim, J.; Lee, M. J.; Son, Y. J.; Jeong, J.; Chung, D. Y.; Lim, A.; Choe, H.; Park, H. S.; Sung, Y.-E. Electrochemical Synthesis of Nanoporous Tungsten Carbide and Its Application as Electrocatalysts for Photoelectrochemical Cells. *Nanoscale* **2017**, *9*, 5413−5424.
(42) Kang, J. S.; Kim, J.; Lee, M. J.; Son, Y. J.; Chung, D. Y.; Park, S.; Jeong, J.; Yoo, J. M.; Shin, H.; Choe, H.; Park, H. S.; Sung, Y.-E. Electrochemically Synthesized Nanoporous Molybdenum Carbide as a Durable Electrocatalyst for Hydrogen Evolution Reaction. *Adv. Sci.* **2018**, *5*, No. 1700601.
(43) McKendry, I. G.; Thenuwara, A. C.; Sun, J.; Peng, H.; Perdew, J. P.; Strongin, D. R.; Zdilla, M. J. Water Oxidation Catalyzed by Cobalt Oxide Supported on the Mattagamite Phase of $CoTe_2$. *ACS Catal.* **2016**, *6*, 7393−7397.
(44) Suryanto, B. H. R.; Zhao, C. Surface-Oxidized Carbon Black as a Catalyst for the Water Oxidation and Alcohol Oxidation Reactions. *Chem. Commun.* **2016**, *52*, 6439−6442.
(45) Wang, W.; Luo, J.; Chen, S. Carbon Oxidation Reactions Could Misguide the Evaluation of Carbon Black-Based Oxygen-Evolution Electrocatalysts. *Chem. Commun.* **2017**, *53*, 11556−11559.
(46) Matsushita, J.; Nakayama, T. Oxidation Behavior of Vanadium Carbide Powder. *J. Adv. Sci.* **1998**, *10*, 97−99.
(47) Camargo, L. G. B.; Palazzo, B. G.; Taylor, G.; Norris, Z. A.; Patel, Y. K.; Hettinger, J. D.; Yu, L. Carbide-Derived Carbon by Electrochemical Etching of Vanadium Carbides. *J. Electrochem. Soc.* **2015**, *162*, H811.
(48) Gilligan, R.; Nikoloski, A. N. The Extraction of Vanadium from Titanomagnetites and Other Sources. *Miner. Eng.* **2020**, *146*, No. 106106.
(49) Shi, H.; Liang, H.; Ming, F.; Wang, Z. Efficient Overall Water-Splitting Electrocatalysis Using Lepidocrocite VOOH Hollow Nanospheres. *Angew. Chem., Int. Ed.* **2017**, *56*, 573−577.
(50) Wan, J.; Wang, C.; Tang, Q.; Gu, X.; He, M. First-Principles Study of Vanadium Carbides as Electrocatalysts for Hydrogen and Oxygen Evolution Reactions. *RSC Adv.* **2019**, *9*, 37467−37473.
(51) Hansen, H. A.; Rossmeisl, J.; K. Nørskov, J. Surface Pourbaix Diagrams and Oxygen Reduction Activity of Pt, Ag and Ni(111) Surfaces Studied by DFT. *Phys. Chem. Chem. Phys.* **2008**, *10*, 3722−3730.
(52) Zhou, H.; Yu, F.; Zhu, Q.; Sun, J.; Qin, F.; Yu, L.; Bao, J.; Yu, Y.; Chen, S.; Ren, Z. Water Splitting by Electrolysis at High Current Densities under 1.6 Volts. *Energy Environ. Sci.* **2018**, *11*, 2858−2864.

https://dx.doi.org/10.1021/acssuschemeng.0c04759
ACS Sustainable Chem. Eng. 2020, 8, 14101−14108